



The Atacama Cosmology Telescope: Systematic Transient Search of 3 Day Maps

Yaqiong Li^{1,2}, Emily Biermann³, Sigurd Naess⁴, Simone Aiola⁵, Rui An⁶, Nicholas Battaglia⁷, Tanay Bhandarkar⁸, Erminia Calabrese⁹, Steve K. Choi^{1,7}, Kevin T. Crowley¹⁰, Mark Devlin⁸, Cody J. Duell¹, Shannon M. Duff¹¹, Jo Dunkley^{12,13}, Rolando Dünner¹⁴, Patricio A. Gallardo¹⁵, Yilun Guan¹⁶, Carlos Hervías-Caimapo¹⁴, Adam D. Hincks^{16,17}, Johannes Hubmayr¹¹, Kevin M. Huffenberger¹⁸, John P. Hughes¹⁹, Arthur Kosowsky³, Thibaut Louis²⁰, Maya Mallaby-Kay²¹, Jeff McMahon^{15,21,22,23,24}, Federico Nati²⁵, Michael D. Niemack^{1,7}, John Orlowski-Scherer²⁶, Lyman Page¹², Maria Salatino^{27,28}, Cristóbal Sifón²⁹, Suzanne T. Staggs¹², Cristian Vargas¹⁴, Eve M. Vavagiakis¹, Yuhan Wang¹², and Edward J. Wollack³⁰

¹ Department of Physics, Cornell University, Ithaca, NY 14853, USA

² Kavli Institute at Cornell for Nanoscale Science, Cornell University, Ithaca, NY 14853, USA

³ Department of Physics and Astronomy, University of Pittsburgh, Pittsburgh, PA, 15213, USA

⁴ Institute of Theoretical Astrophysics, University of Oslo, Oslo, Norway

⁵ Center for Computational Astrophysics, Flatiron Institute, 162 5th Avenue, New York, NY 10010 USA

⁶ Department of Physics and Astronomy, University of Southern California, Los Angeles, CA 90089, USA

⁷ Department of Astronomy, Cornell University, Ithaca, NY 14853, USA

⁸ Department of Physics and Astronomy, University of Pennsylvania, 209 S. 33rd Street, Philadelphia, PA 19104, USA

⁹ School of Physics and Astronomy, Cardiff University, The Parade, Cardiff, Wales CF24 3AA, UK

¹⁰ Center for Astrophysics and Space Studies; University of California, San Diego, SERF Building Room 333; 9500 Gilman Drive, La Jolla, CA 92093-4204, USA

¹¹ National Institute of Standards and Technology, Quantum Sensors Group, 325 Broadway, Boulder, CO 80305, USA

¹² Joseph Henry Laboratories of Physics, Jadwin Hall, Princeton University, Princeton, NJ 08544, USA

¹³ Department of Astrophysical Sciences, Peyton Hall, Princeton University, Princeton, NJ 08544 USA

¹⁴ Instituto de Astrofísica and Centro de Astro-Ingeniería, Facultad de Física, Pontificia Universidad Católica de Chile, Avenida Vicuña Mackenna 4860, 7820436 Macul, Santiago, Chile

¹⁵ Kavli Institute for Cosmological Physics, University of Chicago, 5640 S. Ellis Avenue, Chicago, IL 60637, USA

¹⁶ David A. Dunlap Department of Astronomy & Astrophysics, University of Toronto, 50 St. George Street, Toronto ON M5S 3H4, Canada

¹⁷ Specola Vaticana (Vatican Observatory), V-00120 Vatican City State, Rome, Italy

¹⁸ Department of Physics, Florida State University, Tallahassee, FL 32306, USA

¹⁹ Department of Physics and Astronomy, Rutgers University, 136 Frelinghuysen Road, Piscataway, NJ 08854, USA

²⁰ Université Paris-Saclay, CNRS/IN2P3, IJCLab, F-91405 Orsay, France

²¹ Department of Astronomy and Astrophysics, University of Chicago, 5640 S. Ellis Avenue, Chicago, IL 60637, USA

²² Department of Physics, University of Chicago, 5720 S. Ellis Avenue, Chicago, IL 60637, USA

²³ Enrico Fermi Institute, University of Chicago, 5640 S. Ellis Avenue, Chicago, IL 60637, USA

²⁴ Fermi National Accelerator Laboratory, Batavia, IL 60637, USA

²⁵ University of Milano-Bicocca, Milan, Italy

²⁶ Department of Physics, McGill University, 3600 University Street, Montreal, QC, H3A 2T8, Canada

²⁷ Stanford University, Stanford, CA 94305, USA

²⁸ Kavli Institute for Astroparticle Physics and Cosmology (KIPAC), Stanford, CA 94305, USA

²⁹ Instituto de Física, Pontificia Universidad Católica de Valparaíso, Casilla 4059, Valparaíso, Chile

³⁰ NASA Goddard Space Flight Center, 8800 Greenbelt Road, Greenbelt, MD 20771, USA

Received 2023 March 7; revised 2023 June 28; accepted 2023 July 6; published 2023 October 13

Abstract


We conduct a systematic search for transients in 3 yr of data (2017–2019) from the Atacama Cosmology Telescope (ACT). ACT covers 40% of the sky at three bands spanning from 77–277 GHz. Analysis of 3 day mean-subtracted sky maps, which were match filtered for point sources, yielded 29 transient detections. Eight of these transients are due to known asteroids, and three others were previously published. Four of these events occur in areas with poor noise models and thus we cannot be confident they are real transients. We are left with 14 new transient events occurring at 11 unique locations. All of these events are associated with either rotationally variable stars or cool stars. Ten events have flat or falling spectra indicating radiation from synchrotron emission. One event has a rising spectrum indicating a different engine for the flare.

Unified Astronomy Thesaurus concepts: [Transient sources \(1851\)](#); [Stellar flares \(1603\)](#); [Cosmic microwave background radiation \(322\)](#); [Asteroids \(72\)](#)

1. Introduction

Transient astronomical sources comprise some of the most dramatic and extreme astrophysical events, such as supernovae, binary star mergers, active galactic nuclei (AGNs), gamma-ray

bursts (GRB), and tidal disruption events (TDE). Continuous monitoring of large sky regions to detect transients has been a major motivation behind the upcoming Rubin Observatory (Ivezić et al. 2019) and several other efforts at optical wavelengths, such as the Zwicky Transient Facility (Masci et al. 2018) and ASAS-SN (Christy et al. 2022). Interest in transient astronomy has greatly increased with the first gravitational wave sources detected by LIGO (Abbott et al. 2016), and the detection of sources in both gravitational waves and multiple electromagnetic wave bands. Wide-field

 Original content from this work may be used under the terms of the [Creative Commons Attribution 4.0 licence](#). Any further distribution of this work must maintain attribution to the author(s) and the title of the work, journal citation and DOI.

millimeter wavelength surveys have focused on mapping the unchanging microwave background for cosmological applications, but recently some have reached the combination of the high angular resolution, wide survey area, and sensitivity required to start probing the time-variable millimeter sky.

Synchrotron transient events are often very bright in millimeter wavelengths. For instance, GRB afterglow emission often peaks in millimeter and submillimeter wavelengths (see Granot & Sari 2002). This motivates the application of blind millimeter transient searches as a means to identify GRB orphan afterglows, which is a GRB observed off-axis without any corresponding gamma-ray emission. Such events have been theorized but never observed, highlighting the importance of millimeter transient surveys. Millimeter wavelengths are also sensitive to reverse shock (RS) emission from GRBs. Large-scale millimeter surveys will therefore be able to provide an unbiased estimate of the percentage of long GRBs with RS emission (Eftekhari et al. 2022). Similarly, cosmic microwave background (CMB) surveys will allow us to constrain models of other types of transients such as TDEs. Since millimeter emission from TDEs indicated the presence of synchrotron emission, millimeter transient surveys can also constrain the fraction of TDEs that produce jets (Eftekhari et al. 2022). Wide-field CMB surveys are uniquely poised to answer these science questions as, in contrast to current radio and infrared surveys, they survey large areas of the sky in short periods of time providing a key statistical window into synchrotron transients. In particular, ACT boasts much lower noise levels than previous wide-field submillimeter surveys. Whereas Planck, an all-sky CMB survey, had noise levels on the order of 0.2–1 Jy (Aghanim et al. 2020), ACT has noise levels on the order of tens of millijansky.

In recent years, there have been a growing number of millimeter transient detections from both targeted and blind searches. There have been several follow-up observations done in radio and millimeter wavelengths of extragalactic transients such as that of Kuno et al. (2004) who reported a detection at 90 GHz of the afterglow of GRB 030329 ($z = 0.17$) with a flux around 65 mJ. More than a decade later, Laskar et al. (2019) detected a polarized RS from GRB 190114C at a frequency of 97.5 GHz. Other types of events are also seen in the millimeter wavelength. For instance, Yuan et al. (2016) reported millimeter emission from the TDE IGR J12580+0134. Ho et al. (2019) studied the unprecedented transient AT2018cow in radio and submillimeter bands, finding its emission to be inconsistent with synchrotron emission or Compton scattering of UVIOR photons, indicating a new class of millimeter transients.

Wide-field millimeter surveys can also perform targeted searches of transients by either studying the variability of their own point source catalogs or looking for variability at locations of known transients. Chen et al. (2013) studied the variability of Planck sources in Wilkinson Microwave Anisotropy Probe data. They found 19 sources that were consistent with rotating jet or long-term flaring models and 13 sources that had more complex variability that did not fit into either model. More recently, Hervías-Caimapo et al. (2023) conducted a targeted search for transients in ACT data by stacking observations of known GRBs, TDEs, supernovae, and other transients. They did not detect any of these events in ACT data but provided upper flux limits for each source.

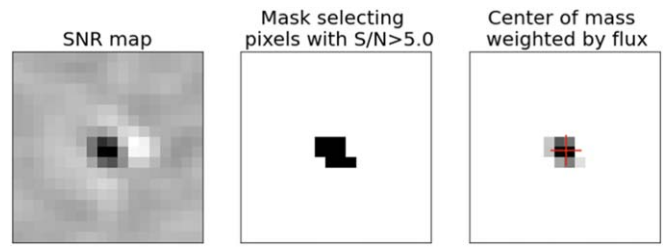


Figure 1. Process of the initial detection, with each plot showing a 0.3×0.3 map. The first step is to make a mask (middle) on the S/N map (left) selecting pixels that have $S/N > 5.0$. The mask is then applied to the flux map (right), and the candidate position, shown as the red cross mark, is evaluated as the center of mass weighted by the flux values within the selected pixels.

Table 1

Summary of the Three Geometric Data Cuts Applied to Each 3 day Map after the Requirement That a Candidate Appear in at Least Two Frequency or Array Combinations is Applied

	Remaining Candidates	Fraction Cut	Fraction of Map Masked
Frequency and array cut	78,367	0.76	...
Neighbor cut	133,119	0.60	0.005
ZiVC cut	88,936	0.74	0.030
Edge cut	278,044	0.17	0.010
All cuts	5020	0.94	0.045

Note. The first column quotes the number of candidates remaining after that cut, the second gives the fraction of all candidates that do not pass these cuts, and the last column gives the fraction of the total number of pixels masked by each cut. Note that these cuts are done in tandem and are independent of each other. The neighbor cut removes candidates with neighbors in the same map within $20'$, the zero inverse variance contour (ZiVC) cut masks candidates within 5 pixels of zero inverse variance contours, and the edge cut masks candidates within 5 pixels of the edge.

There have also been several blind searches for transients in millimeter wavelengths. In 2016, the South Pole Telescope (SPT) reported one candidate event observed during the 2012–2013 season at a 2.6σ significance with a peak flux of 16.5 ± 2.4 mJy in the 150 GHz band. This event was broadly consistent with a GRB orphan afterglow. Although a statistical fluctuation could not be ruled out, the event’s spectra and polarization were consistent with a small-volume synchrotron source such as a GRB or another jet-producing event. The absence of a spatial correlation with known point sources suggests that this event was not an AGN flare but rather an off-axis GRB that is an *orphan afterglow* (Whitehorn et al. 2016). More recently, Guns et al. (2021) performed a transient search with the updated SPT-3G telescope yielding the detection of two additional extragalactic events with durations on the order of weeks. Curiously, these events did not have obvious galactic associations. The authors suggest that the events may be from AGN activity but the data are inconclusive.

Most blind transient searches in the millimeter also detect stellar flares from galactic sources. ACT serendipitously discovered three bright transient sources coincident with stars (Naess et al. 2021a) and SPT reported 13 transients most likely due to stellar flares (Guns et al. 2021). Millimeter stellar flares have also been reported in other works such as those of Bower et al. (2003), Brown & Brown (2006), Massi et al. (2006),

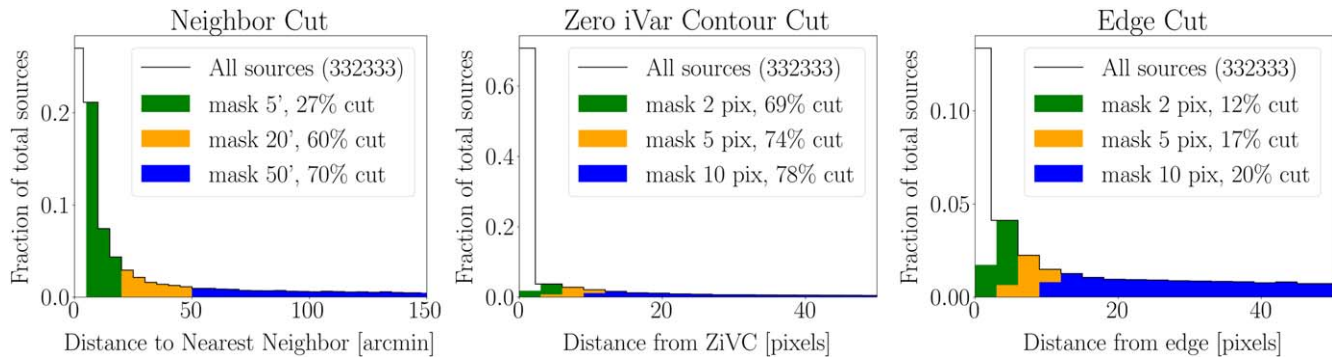


Figure 2. Left: histogram of the distance to each detection’s nearest neighbor with a bin size of $5'$. The peak close to zero indicates there are clusters of spurious detections in many of the maps so we cut any candidate with a nearest neighbor of $20'$ or less. Center: histogram of each candidate’s distance from the nearest zero inverse variance contour, defined to be an inverse variance of less than 1.5×10^{-5} K, with a bin size of 3 pixels. There is a large peak of candidates near zero inverse variance contours, which drops after 3 pixels. We mask out to 5 pixels, cutting 74% of all sources. Right: histogram of each candidate’s distance from the map edge in pixel units with a bin size of 3 pixels. As expected, there is an excess number of candidates near the edge of the map as the map edges are noisy and so appear variable when sampled every 3 days. At a mask size of 5 pixels, we cut off the peak of candidates near the edge.

Mairs et al. (2019), and MacGregor et al. (2020). These flares are most likely due to stellar magnetic field reconnection.

In this work, we complete a systematic search for transient events with 3 yr of ACT data using spatial maps each containing about 3 days worth of time-integrated data. In Section 2, we introduce the ACT survey and the maps used for this analysis. In Section 3, we describe how the transient events are detected and how data cuts are applied to the sample. In Section 4, we present our findings and possible counterparts for each transient. After all cuts are applied we are left with 29 events, which we then analyze in the time domain to further constrain the timescale of each event. Three of these events are re-detections from Naess et al. (2021a), eight appear to be from asteroids that were not masked in the 3 day maps, and four occur in areas with poor noise models and cannot be confirmed as real transients. This leaves 14 new transient detections at 11 unique positions on the sky. Most of the events have clear stellar associations. In Section 5, we summarize the nature of these counterparts.

2. Data

The Atacama Cosmology Telescope (ACT) was a 6 m off-axis Gregorian telescope located in the Atacama Desert in Chile at an altitude of 5200 m (Fowler et al. 2007). AdvACT was the third-generation ACT instrument. It simultaneously housed three optics tubes with a total field of view spanning $\sim 1.5^\circ$ (Thornton et al. 2016), each containing a set of lenses, low-pass filters, and a single AdvACT detector array (Ho et al. 2017; Choi et al. 2018). The ACT data set considered here covers the three bandpasses f090 (77–112 GHz), f150 (124–172 GHz), and f220 (182–277 GHz) using the three dichroic polarization-sensitive transition edge sensor bolometer arrays PA4 (f150+f220), PA5 (f090+f150), and PA6 (f090+f150). The beams’ FWHM are $2.0'$, $1.4'$, and $1'$, respectively, for bands f090, f150, and f220.

During observations, the telescope scanned the sky in azimuth at a fixed elevation at a scan speed of $\sim 1.5^\circ \text{ s}^{-1}$. When the sky was rising, it took ~ 6 minutes for a point on the sky to be gradually swept across by the detectors in PA4 and PA5. Then, after ~ 3 minutes this process would repeat for the detectors in PA6. This order was reversed when the sky was setting. The bolometer signals, i.e., measured optical power fluctuations, were stored in time-ordered data (TOD) files, each

containing a roughly 10 minute time series for all detectors in a single array. A selection process was applied to TOD data to cut off defective detectors or dark detectors that were not optically coupled to the sky signal. The data were then calibrated to sky temperature fluctuations using calibration observations on planets with known temperature models, such as Saturn and Uranus. The TOD was then ready to be made into maps with pointing functions that associate time stamps to locations on the sky. The detailed data selection and calibration process is described in Aiola et al. (2020).

We search for transient events using 3 day maps and filtering strategies originally created to search for Planet 9 (Naess et al. 2021b). The search covered $180,000 \text{ deg}^2$ of the sky using ACT data taken from 2017–2019. Although these maps were not designed for a systematic transient search, their short timescale is well suited for this purpose. Since the beam and pointing of the daytime (UTC 11–23) observations are more affected by the Sun, the maps are made separately by the TODs chunks spanning for approximately 3 days taken during daytime and nighttime by each of the three detector arrays at each of the two frequency bands. Therefore, there are 12 maps (day and night time data within three arrays with two bands) for each 3 day period. As described in Dünner et al. (2012), the beam-convolved intensity map m , in CMB temperature units of microkelvins, is the solution in

$$d = Pm + n, \quad (1)$$

where d is the TOD, P is the pointing matrix, and n is noise from instruments and atmosphere that is modeled with covariance matrix N . We use the maximum-likelihood mapmaking method that maximizes the likelihood

$$L = \exp \left[-\frac{1}{2} (d - Pm)^T N^{-1} (d - Pm) \right] \quad (2)$$

with the standard solution being

$$\hat{m} = (P^T N^{-1} P)^{-1} P^T N^{-1} d. \quad (3)$$

For each 3 day map, a mean sky subtraction at the corresponding frequency band is implemented so only the time-varying signal remains. Regions within 0.8° of the planets (according to Aiola et al. 2020, a typical distance between sidelobes and planets is approximately $47'$) and within $3'$ (3 times the largest beam FWHM) of the bright asteroids are

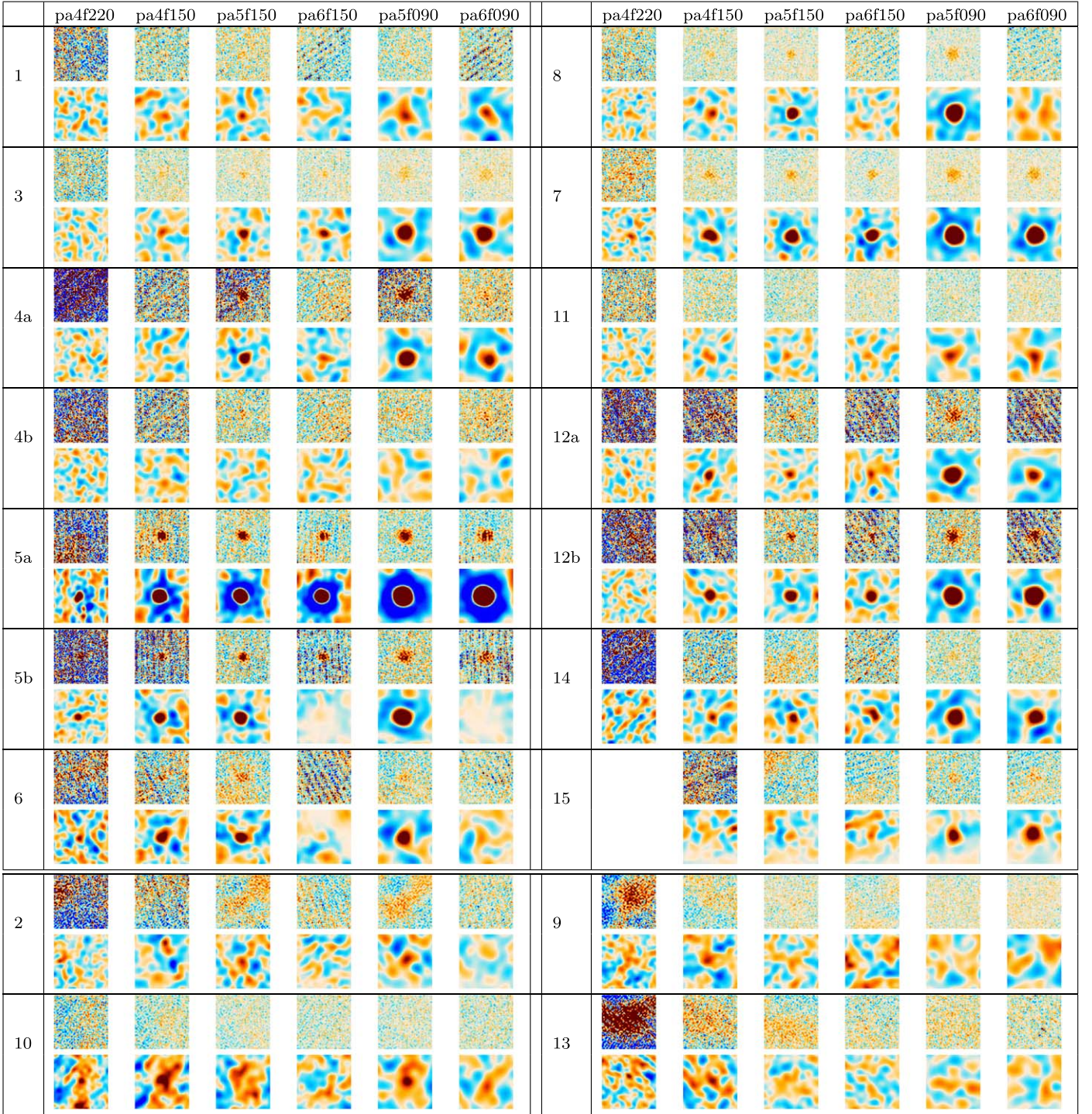


Figure 3. $10' \times 10'$ 3 day thumbnail maps for each transient. The upper row represents the intensity map with a $\pm 5000 \mu\text{K}$ color range. The bottom row represents the S/N map after applying a matched filter, with a ± 5 color range. Due to the conjugate gradient iteration used to solve the maximum-likelihood mapmaking equation only being run for 10 steps, these maps are effectively mildly high pass filtered. The affected scales have negligible weight in the matched filter. Events 2, 9, 10, and 13 at the bottom of the table represent the four events that are difficult to determine if they are real transients.

masked to avoid contamination from planet sidelobes and false transient detection from known moving astronomical objects. The map is then matched and filtered to look for point sources and gives an estimation of flux density F and signal-to-noise ratio (S/N) at each pixel as

$$F = \frac{\rho}{\kappa} = \frac{B^T U^{-1} \hat{m}}{\text{diag}(B^T U^{-1} B)} \quad (4)$$

$$S/N = \frac{\rho}{\sqrt{\kappa}} = \frac{B^T U^{-1} \hat{m}}{\sqrt{\text{diag}(B^T U^{-1} B)}} \quad (5)$$

where κ and ρ are, respectively, the inverse variance and inverse variance weighted flux density. B is the response matrix that takes a single pixel in flux density unit to beam-convolved structures in the CMB temperature unit. U is the covariance matrix of noise u in \hat{m} , but different from noise n in

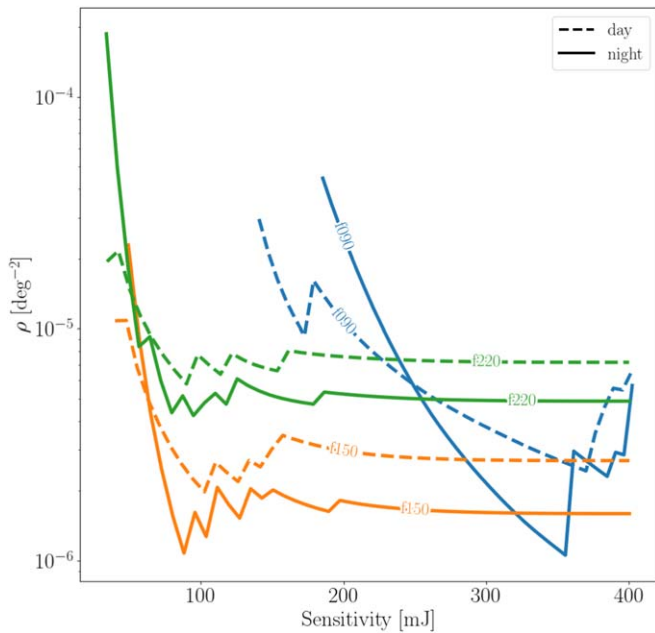


Figure 4. Surface density of transients for each frequency split between day and night data. The surface density is found by counting the number of transients we are able to detect given the sensitivity level divided by the map area at that sensitivity or lower.

Table 2
Transient Surface Density for Each Frequency Split between Day and Night Data

Frequency	ρ [deg ⁻²] Day	ρ [deg ⁻²] Night
f090	6.52e-06	5.69e-06
f150	2.70e-06	1.59e-06
f220	7.18e-06	4.88e-06

Note. These values represent the surface density for the highest sensitivity required to detect one of our transients. We split this measurement between frequencies and day and night data since the sensitivity thresholds of these maps are very different. The average transient surface density across all frequencies and arrays is 7.06×10^{-6} [deg]⁻².

Equation (1), u considered here is everything that is not a point source, including instrumental and atmospheric noise, clusters, and CMB signals. Detailed methods and noise models for 3 day maps are described in Naess et al. (2021b).

Since the 3 day maps were made as part of a search for Planet 9, some trade-offs are made that are suitable when performing large stacks of maps, but at times not ideal when analyzing maps in isolation. In particular, the maps' matched filter numerator was computed directly in the time domain while the denominator was computed in map space. This approach is fast, but only accurate if the time-domain noise model and map-space noise model are consistent. In practice, this is an approximation, which introduces a bias in areas where the map's hit density changes rapidly from pixel to pixel. This does not happen when performing large stacks like in the Planet 9 search, but it is quite common when looking for objects in the individual 3 day maps, resulting in many spurious detections (see Section 3.1). Furthermore, the matched filtered 3 day maps are stored at 1' resolution, which was an acceptable performance trade-off for the Planet 9 search (where this was a minor contribution to the overall smoothing budget), but is

suboptimal for blind transient detection. The ways in which the position uncertainty introduced by the selected resolution are handled is detailed in Section 4.2. We plan to resolve these deficiencies in a future paper using maps tailored for transient detection.

3. Methodology

3.1. Initial Detection and Spurious Candidate Cuts

Any pixel or group of pixels with $S/N > 5$ in the 3 day sky-subtracted maps is considered a transient candidate. For each set of 3 day S/N and flux density maps, we first mask pixels with $S/N < 5$, then apply this mask to the corresponding flux density map (Figure 1). The positions of candidates are evaluated to be flux-weighted centroids. We then crossmatch each candidate between detector arrays with a matching distance of $1/5$, which is 1.5 times the resolution of the 3 day maps. We only keep candidates that appear in at least two frequency and array combinations. This cuts 76% of the initial detections.

Even with this cut applied, there are still many spurious detections grouped in clusters and along map edges. Given that 7.8 billion pixels are searched for each combination of array and frequency band, we expect to find around 28,000 false detections in total assuming a Gaussian distribution with the 5σ detection threshold (0.00006%). The probability will be squared to have a false detection at the same or adjacent pixels on different maps. In ideal situations, the false detection would be negligible after crossmatching catalogs from different arrays in the same 3 day period. However, due to the bias and estimation in the mapmaking and filtering process described in Section 2, this initial detection finds 332,333 candidate events, which is a magnitude higher than expected. We perform three additional geometric cuts, requiring a candidate to be cut in all detected frequency and array combinations to exclude it from the analysis. The results of these cuts are summarized in Table 1.³¹ We apply these cuts in tandem with the frequency and array requirement, thus the following statistics include all candidates.

The first geometric cut is motivated by the observation that many of the 3 days exhibit a striped pattern of spurious detections along the scanning direction. These false detections are caused by a systematic underestimation of the inverse variance (i.e., the κ maps mentioned in Section 2) when the coverage is uneven due to low hit counts. The stripe regions are reliably identified by searching for detections with nearby neighbors within the same 3 day map. This approach is motivated by the left-hand plot in Figure 2, which shows a histogram of each candidate's nearest neighbor: there is a clear excess of detections with neighbors within $\sim 1^\circ$, which would not be expected for real detections since extragalactic transients should be spatially uncorrelated. Based on this histogram, we cut any candidates with a neighbor within $20'$ as there is an overdensity of detections with the closest neighbor within this range. This cut removes 60% of all candidates.

We see a similar striped pattern along zero inverse variance contours. During the mapmaking process, some approximations result in streaks of spurious detections with vanishing inverse variance and therefore a high S/N . In the center plot in Figure 2, we plot a histogram of the candidates' distances from

³¹ Note that a candidate might be cut by more than one criterion.

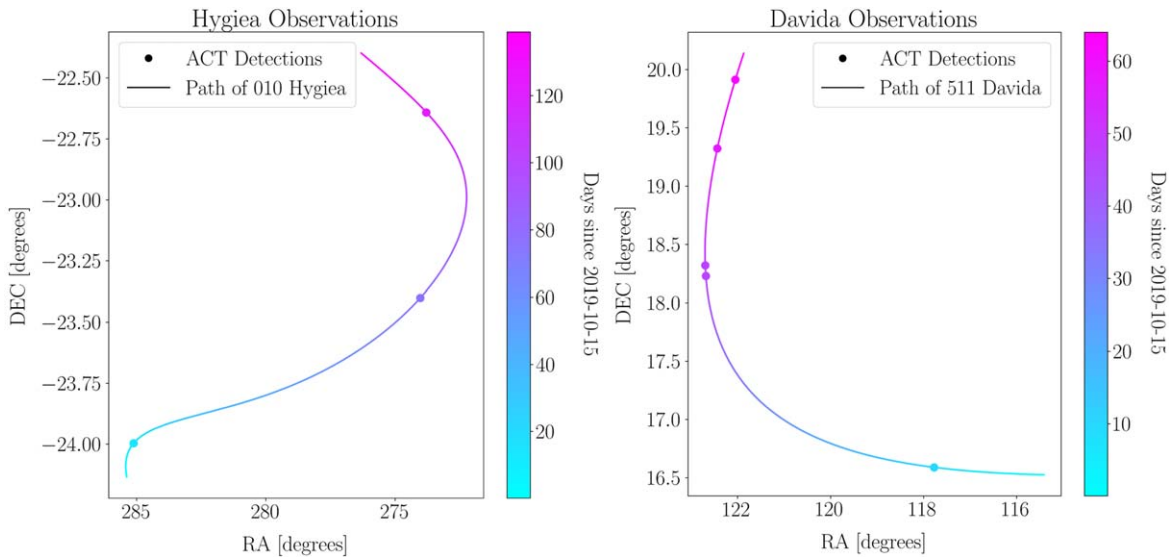


Figure 5. Left: the three transient events consistent with Hygiea observations. Right: the five transient events consistent with Davida observations. All of the plotted positions and observation times are consistent with the asteroids' paths. The position errors are on the order of $0''.1$.

Table 3
Eight Events Associated with Asteroids

Name	R.A. $^{\circ}$	Decl. $^{\circ}$	Pos. Acc $''$	Peak Flux (mJy)			Mean Flux (mJy)			Peak Time (UTC)	α
				f220	f150	f090	f220	f150	f090		
Hygiea(a)	285.1166	-23.9962	14	334 ± 71	199 ± 21	104 ± 20	1.4 ± 4.0	1.3 ± 1.5	0.8 ± 2.6	2017-05-21 04:27	1.4 ± 0.3
Hygiea(b)	274.0251	-23.4008	5	369 ± 42	218 ± 18	92 ± 20	19.1 ± 6.7	3.0 ± 2.6	0.5 ± 4.6	2017-07-24 05:50	1.5 ± 0.2
Hygiea(c)	273.7942	-22.6426	10	351 ± 52	144 ± 20	65 ± 19	18.5 ± 7.3	8.5 ± 2.8	-0.2 ± 5.0	2017-09-9 02:54	2.1 ± 0.4
Davida(a)	117.7733	16.5879	8	206 ± 34	114 ± 15	53 ± 14	4.0 ± 2.1	1.9 ± 0.8	-1.9 ± 1.4	2019-10-24 09:01	1.6 ± 0.3
Davida(b)	122.6793	18.2278	5	277 ± 32	155 ± 13	57 ± 12	-0.8 ± 2.1	0.2 ± 0.8	4.0 ± 1.4	2019-11-30 07:12	1.8 ± 0.2
Davida(c)	122.6946	18.3167	8	192 ± 39	118 ± 16	57 ± 13	-2.2 ± 2.0	0.3 ± 0.8	3.1 ± 1.3	2019-12-1 08:57	1.6 ± 0.4
Davida(d)	122.4329	19.3231	2	343 ± 27	162 ± 14	86 ± 10	5.1 ± 2.0	1.1 ± 0.7	3.3 ± 1.3	2019-12-11 06:45	1.7 ± 0.2
Davida(e)	122.0468	19.9151	6	313 ± 44	174 ± 16	62 ± 15	-5.1 ± 1.9	0.8 ± 0.8	1.8 ± 1.4	2019-12-16 05:10	1.8 ± 0.3

a zero inverse variance region and cut any candidate within 5 pixels of these features (about 74% of all candidates).

Lastly, we cut any candidate near a map edge. Map edges are especially noisy and appear to be variable when sampled every 3 days. In the right-hand plot in Figure 2, we plot a histogram of the pixel distance of each candidate from the edges of the map. We see a spike in candidates within 5 pixels from the edge of the map and so we mask this region. This cut applies to 17% of all candidates.

After these cuts are applied an internal crossmatch is performed to find repeating events. Candidates with positions within $1'$ of each other are considered the same object. This leaves us with 667 independent candidates.

3.2. Candidate Verification

For each of the 667 candidates, we calculate the mean flux by applying a matched filter to the mean sky map using data from 2017–2021, and mask candidates with mean flux >50 mJy or <-50 mJy. The high-mean-flux candidates are likely variable point sources such as AGN or dusty star-forming galaxies. These high-mean-flux candidates are already detected in our standard point source catalogs, and there are dedicated studies in preparation on the light curves of these candidates. In this paper, we will concentrate on candidates that are not detectable in the mean sky maps. The candidates with negative mean fluxes are located close to bright point sources.

Table 4
Properties of the Transient Events^a

Ind	Name	R.A. °	Decl. °	Pos.	Peak Flux (mJy)			Mean Flux (mJy)			Time			α
					f220	f150	f090	f220	f150	f090	Peak (UTC)	Rise	Fall	
1	J060702 +174157	91.7603	17.6993	22	36 ± 35	78 ± 13	64 ± 14	-1.2 ± 2.3	-2.3 ± 0.9	-4.6 ± 1.6	2017-09-05 05:35	<43 minutes	<25 hr	0.0 ± 0.5
3	J224500 -331532	341.2510	-33.2589	14	192 ± 41	253 ± 20	255 ± 12	5.5 ± 2.3	4.4 ± 0.8	8.8 ± 1.4	2017-10-08 18:17	<1 day	>23 minutes	-0.6 ± 0.2
4a		343.2597	16.8408	8	1036	1154	801				2018-09-10 21:55		<2 days	0.5 ± 0.1
4b	J225302 +165027				± 122 -15 ± 58	± 52 141 ± 20	± 34 148 ± 18	4.7 ± 3.2	7.8 ± 1.1	18.7 ± 2.0	2019-06-06 04:18	<2 days	<3 days	-0.6 ± 0.4
5a		292.1328	-35.1327	3	2496	2383	1525				2018-10-04 02:22	<1 day	<20 days	0.9 ± 0.05
5b	J192831 -350757				± 177 545 ± 69	± 40 645 ± 23	± 27 490 ± 20	4.7 ± 3.7	11.7 ± 1.4	37.2 ± 2.7	2019-08-10 23:10	<3 days	>1 day	0.4 ± 0.1
6	J190222 -53610	285.5938	-5.6028	10	926 ± 87	717 ± 34	350 ± 29	12.7 ± 5.6	5.3 ± 2.1	7.7 ± 3.9	2018-10-20 20:32	<1 day	<1 day	1.2 ± 0.1
7	J085813 +194546	134.5579	19.7630	4	103 ± 31	197 ± 9	269 ± 9	3.0 ± 1.9	0.1 ± 0.8	2.4 ± 1.5	2018-11-15 05:18	<5 days	<22 hr	-0.8 ± 0.1
8	J142555 +141207	216.4831	14.2020	8	446 ± 61	563 ± 17	562 ± 14	-0.5 ± 1.9	1.7 ± 0.6	5.6 ± 1.1	2018-11-21 08:07	<20 hr	>23 hr	-0.1 ± 0.1
11	J060757 -542626	91.9890	-54.4408	20	108 ± 65	113 ± 21	113 ± 15	-3.6 ± 2.6	0.8 ± 1.0	2.6 ± 2.1	2019-08-09 12:18	<24 hr	<18 hr	0.0 ± 1.6
12a		54.1961	0.5865	5	108	302	448				2019-08-10 13:35	<30 hr	>23 hr	-1.1 ± 0.2
12b	J033647 +03511				± 66 356 ± 67	± 26 487 ± 23	± 25 580 ± 21	11.7 ± 4.0	11.9 ± 1.5	30.1 ± 2.8	2019-09-28 10:23	>2 days	<2 days	-0.5 ± 0.1
14	J125045 +113338	192.6887	11.5607	14	76 ± 114	202 ± 29	218 ± 21	-1.8 ± 1.8	1.8 ± 0.6	5.4 ± 1.2	2019-09-17 11:34	<1 day	<49 days	-0.3 ± 0.4
15	J180723 +194222	271.8483	19.7063	14	NA	82 ± 24	153 ± 19	0.5 ± 2.2	2.8 ± 0.8	5.5 ± 1.6	2019-11-13 13:01	<6 days	<12 days	-1.4 ± 0.7
N1	J181515 -492746	273.8166	-49.4627	5	NA	555 ± 28	282 ± 18	-2.5 ± 5.7	6.4 ± 2.2	16.0 ± 4.7	2019-11-08 17:22	>8 minutes	>4 minutes	1.3 ± 0.2
N2	J070038 -111436	105.1588	-11.2458	10	NA	344 ± 30	152 ± 21	-1.8 ± 7.2	5.5 ± 2.7	4.5 ± 5.2	2019-12-14 21:30	<8 days	>8 minutes	1.9 ± 0.5
N3	J200758 +160954	301.9965	16.1642	7	222 ± 53	300 ± 26	346 ± 18	-2.2 ± 3.0	2.7 ± 1.1	15.4 ± 2.1	2018-09-11 19:36	<1 day	>3 days	-0.4 ± 0.2
2		316.0950	-13.6699	20	NA	1050	1311	0.9	-2.7	-2.0	2017-09-27	<6 minutes	<1 day	-0.5

Table 4
(Continued)

Ind	Name (ACT-T)	R.A. °	Decl. °	Pos. Acc. ^a	Peak Flux (mJy)			Mean Flux (mJy)			Time			α
					f220	f150	f090	f220	f150	f090	Peak (UTC)	Rise	Fall	
					± 56	± 30	± 4.5	± 1.6	± 3.0	00:21			± 0.1	
9	196.7753	16.6089	21	168	117	12	0.6	0.0	1.2	2019-07-19	<3 hr	>22 hr	2.1	
					± 52	± 19	± 1.7	± 0.6	± 1.1	19:23			± 0.6	
10	208.4267	6.7745	23	293	200	110	-1.5	0.2	0.3	2019-08-05	<19 hr	<1 day	1.2	
					± 57	± 21	± 2.0	± 0.7	± 1.3	14:40			± 0.3	
13	60.9932	14.0094	26	920	542	603	-2.1	1.7	1.2	2019-08-14	<5 minutes	<2 minutes	1.6	
					± 103	± 52	± 3.3	± 1.2	± 2.3	09:27			± 0.2	

Note. Three single detections labeled as “N” are the re-detections of the transients published in Naess et al. (2021a). It is difficult to fit for rise and fall time using light curves due to uneven scanning cadence. Instead, we examine if the scan right before and after the scans with the peak flux density has a $>5\sigma$ detection, and calculate the time interval in between the scans. The rise time of Event 4a is left empty because the time gap between the peak scan and the scan right before is longer than 50 days. The spectral index is evaluated as described in the text, using array-wise flux density values, except for candidate 13. This transient event completed the rise and fall process within the time the sky took to drift across the array. We therefore evaluate the spectral index using flux values taken by only one quarter of detectors in each array, to capture the peak flux.

^a The candidates are listed in the order of the detection time (or the detection of the first event for the repeating candidates).

The flux density around this region is negative due to the effect of the matched filter that acts as a high pass filter, and will increase when the flux of the corresponding point source decreases, resulting in a false detection. There are 82 candidates left after applying the cut on mean flux. We then make light curves to confirm these detections, requiring an $S/N > 3.5$ in at least two arrays or in one array at both frequency bands. These light curves are made from forced photometry, which gives a per-detector flux and flux error, and then evaluates a weighted mean flux as the array-wise result at each frequency band for each scan. This analysis further cuts 41 candidates.

For the rest of the candidates, we made $2^\circ \times 2^\circ$ intensity maps (shown in Figure 3) from TODs covering a 3 day period (or shorter if the scanning cadence is especially high) centered on each event. These maps, referred to as *thumbnail maps*, have $0.25'$ resolution and are centered at the candidate positions. We visually inspected these maps both before and after matched filtering³² and remove candidates with an extended or irregular shape, since we expect all our transients to be point sources. This issue may be caused by poor data quality causing arcminute scale fluctuations. This step is done manually since the number of candidates left is small, but a future effort will be dedicated to developing an automatic process of point-source classification. For some of the remaining candidates, we observed that the raw and filtered maps appear discrepant with each other, e.g., a supposedly strong detection having no visible counterpart in the maps before filtering; or there was an overdensity of $>3\sigma$ peaks near the event in the filtered maps, which should not happen if the noise model is correct. Different from other confirmed false candidates, switching to different noise modeling methods would improve the overdensity issue and the candidates' shape at the expense of decreasing the S/N in the signal. Therefore,

we do not discard these events, but classify them as low-quality candidates.

4. Results

After all cuts are applied, we are left with 29 transient detections. Eight of these events are due to asteroids (see Section 4.2), three were previously detected, and four are low-quality candidates. In this section we use this event rate to calculate the transient surface density of ACT (Section 4.1), characterize the properties of each event, (Section 4.2), and look for counterparts by crossmatching the positions with other surveys (Section 4.3).

4.1. Transient Surface Density

We estimate the surface density of transients in ACT's field of view following the method outlined in Rowlinson et al. (2022). Note that for the following calculations, we only include 14 strong transient candidates. We calculate the sky area in each frequency band and array by dividing maps with the edge and zero inverse variance contour cuts applied into 0.5×0.5 tiles. The surface density, ρ is then $T/(0.25 \text{ deg}^2 N)$ where T is the number of transients we observe and N is the average number of tiles across all frequency and array combinations. We find the transient surface density for this analysis to be $7.06 \times 10^{-6} [\text{deg}]^{-2}$.

We also provide the surface density as a function of sensitivity using the method described in Rowlinson et al. (2022). First, we split the maps by frequency and day/night data as the variance in each of these maps differs significantly. We find the root mean square (rms) noise in each $0.5'$ tile and split the values into 50 bins. The sensitivity of each bin is simply the noise multiplied by our 5σ detection threshold. The surface density is calculated by finding the cumulative area of each bin and the cumulative number of transients detectable at each sensitivity level. The results are shown in Figure 4 and are summarized in Table 2. The table quotes the surface density of

³² This is pure map-space matched filtering, which should be more accurate than the mixed TOD-level/map-space matched filtering used in the main 3 day maps used for the initial search, but still depend on an accurate noise model.

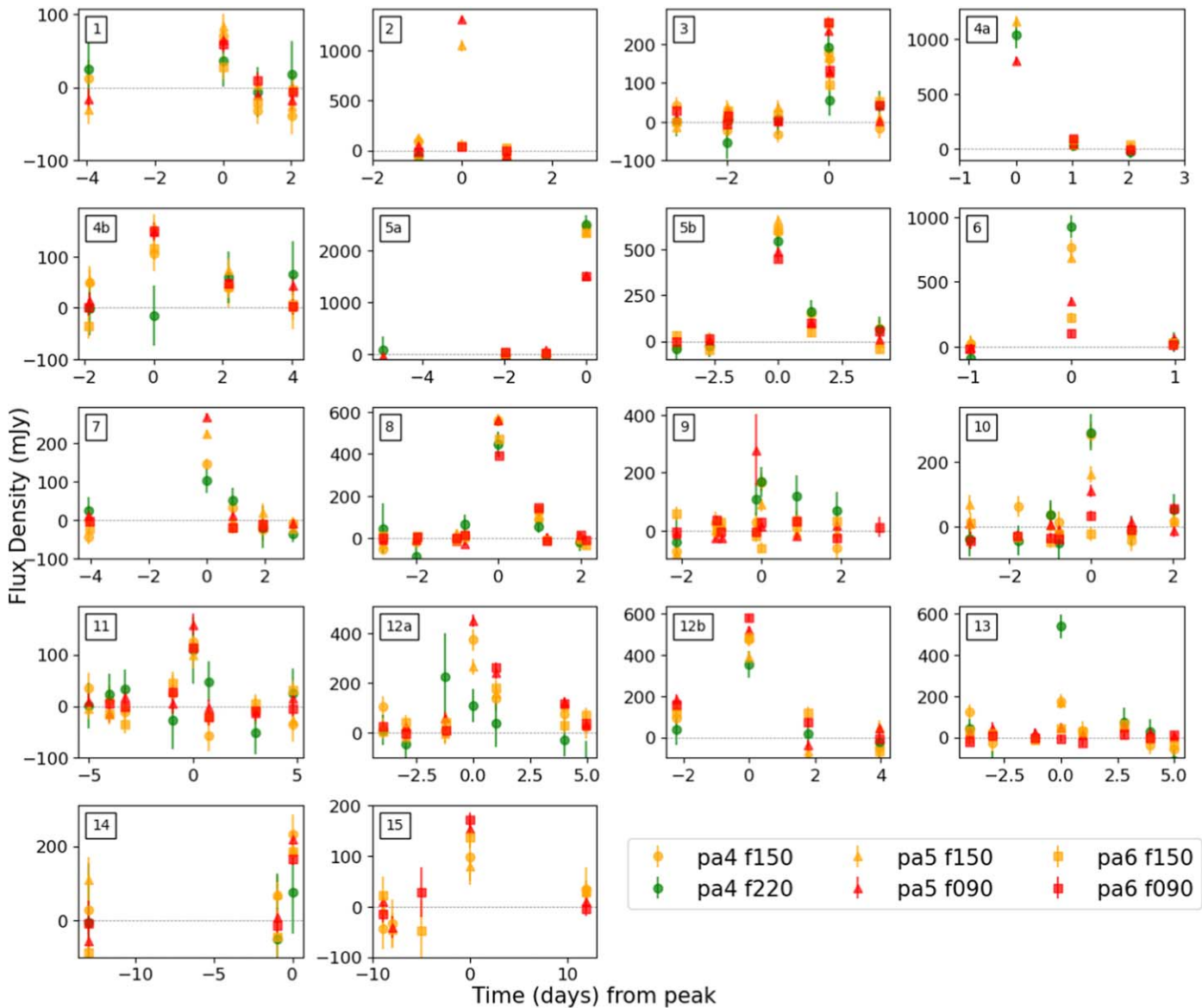


Figure 6. Light curves for 18 detected transient events on day timescales from the peak. Each frequency is denoted by a different color. We see that in most cases the peak is correlated with all frequencies.

the highest sensitivity bins. Note that most of these values are lower than the total surface density quoted above as these calculations only include transients found during the day or night of each frequency band.

We can most directly compare ACT’s transient surface density to the transient survey conducted by SPT-3G (Guns et al. 2021) since ACT and SPT observe in similar wave bands. SPT observes a 1500 deg^2 footprint of the sky every 16 hr. The transient search yielded 15 events over 3500 hr of observations. Therefore, the transient surface density of SPT-3G is roughly $4.57 \times 10^{-5} \text{ deg}^{-2}$, over an order of magnitude higher than ACT. This difference can be explained in a few ways. The SPT-3G transient search has noise levels on the order of 5 mJy, which is much lower than the noise levels for this survey (around 15 mJy). In addition, we expect to overcut many real transients due to the map approximations causing false detections at low hit counts. Finally, ACT surveys a much larger sky area with a less regular cadence than SPT, which also results in missing stellar flare events. Whereas SPT will

reobserve the same location once every day, ACT’s cadence varies from less than 1 day to 2 weeks. We are therefore most sensitive to transients with flare durations on the order of days. We indeed find that most of our detected transients flare on this timescale.

4.2. Characterization

Two groups of our transient events appeared to be close in time and space to each other (see Table 3). Using the IAU Minor Planet Center NEOChecker webtool,³³ we found three events to be coincident with asteroid 10 Hygiea and five events to be coincident with asteroid 511 Davida. In Figure 5, we plot the paths of these asteroids with our events overlaid. All eight events appear consistent in space and time with the asteroid observations which were not masked in our maps. For future blind transient searches, we must be prepared for the possibility of detections from moving objects such as asteroids. This will

³³ See <https://minorplanetcenter.net/cgi-bin/checkneo.cgi>.

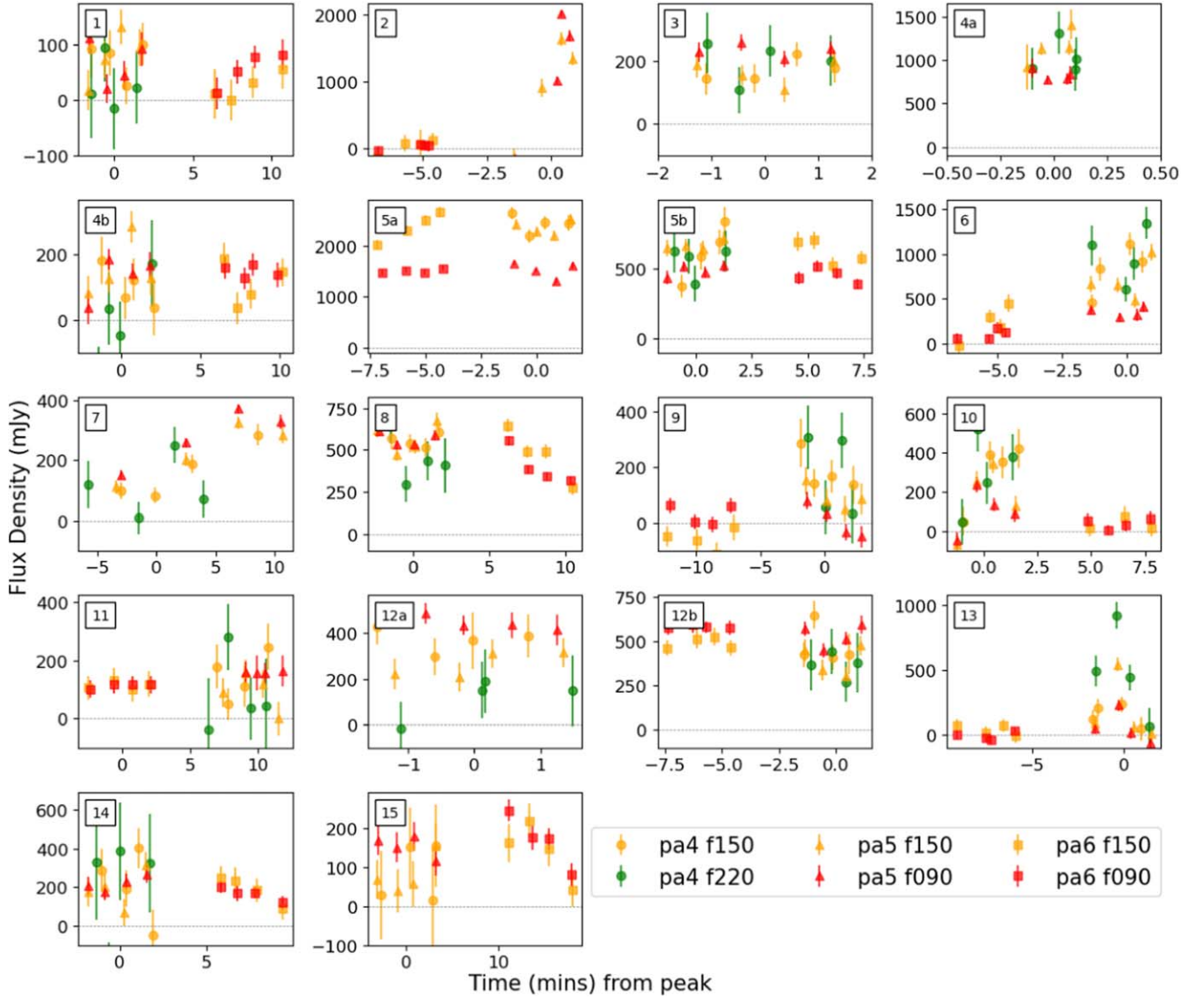


Figure 7. High-resolution light curves for transient events on minute timescales. Events 1, 2, 5, 6, 7, 8, 9, 10, 13, 14, and 15 show strong signal variation within a space of 4 minutes.

become especially important for real-time follow-up observations. A paper dedicated to studying asteroids in ACT data is under review (Orlowski-Scherer et al. 2023).

The properties of the remaining 21 transient events are shown in Table 4. Three single detections labeled as “N” were previously published in Naess et al. (2021a). Among the newly detected events, 12 are single events and three repeat twice, with time intervals ranging from 1 month to 1 yr. The low ($1'$) resolution of the 3 day maps potentially increases the candidates’ position error, so we reestimate the candidate positions using a method similar to the one used in the initial detection on the higher-resolution thumbnail maps described in Section 3.2. We first subtract the corresponding f220/f150/f090 mean sky map and apply a matched filter. The final position for each candidate is the inverse-variance-weighted average among individual positions, using the ratio between the half maximum of the beam and the appropriate S/N as weights. The position accuracy is evaluated by the square root of the variance of the weighted mean. As mentioned in Section 3.2, four out of the 12 single events are difficult to determine if they are real transients due to unusual noise patterns on the intensity

maps. We present these events at the bottom of the table without assigning a formal name.

Flux densities for each scan are evaluated at the refined positions and used to generate light curves (Figure 6) using the same method described in Section 3.2. Higher-resolution light curves (Figure 7) are made by dividing detectors in each array into four groups by the order of observation time to study the minute-by-minute change in flux density. When the flux density values are available in both bands of PA4 and PA5, the spectral index α is evaluated by the best fit of a power law $S_\nu \propto \nu^\alpha$ of frequency ν to the flux measurement S_ν at the three different bands, taking into account the variance of each band flux. Under this circumstance, PA6 is omitted because it scans across the candidates approximately 10 minutes earlier (or later when the sky is rising) than PA4 and PA5. Events 2 and 15 do not have f220 measurements, so α is directly calculated by

$$\alpha = \frac{\log(S_{\nu_1}) - \log(S_{\nu_2})}{\log(\nu_1) - \log(\nu_2)}, \quad (6)$$

Table 5
Possible Counterparts for Each Transient Event from the SIMBAD Database.^b

Name	ID	Object Type	Magnitude	Pos Err (")	Sep (")	Chance
1	V* CP Ori	Eclipsing binary, G0	10.52	22	8.60	5.66e-04
3	V* TX PsA	Eruptive variable, M5IVe	11.84	14	4.24	1.21e-04
4a/b	V* IM Peg	RS CVn variable, K2III	5.66	8	1.48	4.23e-08
5a/b	HD 182928	Rotating variable, G8IIIe	9.37	3	2.15	5.79e-06
6	** SKF 1810A	Young stellar object candidate	12.73	10	7.00	5.05e-03
7	G 9-38	High proper motion binary, M7V/M8Ve	12.49/11.97	4	4.03	1.56e-04
8	StKM 1-1155	Low-mass Star, M0.0Ve	10.91	8	2.71	1.78e-05
11	V* TY Pic	RS CVn variable, G8/K0III+F	7.29	20	6.80	9.82e-06
12a/b	HD 22468	RS CVn variable, K2:Vnk/K4	5.60/8.51	5	4.10	2.59e-07
14	Gaia DR2 3927810990205301504	Star	12.43	14	2.88	5.96e-05
15	HD 347929	Rotating variable, K0	9.04	14	7.66	8.04e-05
N1	2MASS J18151564-4927472	High proper motion star, M3	11.72	5	4.25	5.47e-04
N2	HD 52385	Star, K0/IIII	8.11	10	7.46	5.15e-05
N3	HD 191179	Spectroscopic binary, G5	7.96	7	7.05	4.41e-05
2	Gaia DR2 6885400713762009216	Star	16.74	20	13.02	5.96e-02
9	Gaia DR2 3936693910286240000	Star	13.87	21	33.51	2.11e-02
10 ^a	1636148068921376768	AGN	...	23	17.40	1.20e-02
13	Gaia DR2 38908044312695424	Star	14.34	26	23.58	2.51e-02

Note. The chance of a false association is calculated using the density of Gaia sources with the same magnitude or brighter of the counterpart. If the Gaia object is not found in the SIMBAD database, then the Gaia identification number is listed. All separations are calculated using the Gaia coordinates. This table also includes counterparts associated with the three previously published ACT transients from Naess et al. (2021a). When two stars from the same system are resolved, as is the case with events 7 and 12, we quote the average separation weighted by 1 minus the chance association and we list the lowest of the two chance associations.

^a Field too dense to identify stellar counterpart.

^b If known, the spectral type is given next to the object type.

using the f150 and f090 flux measured by PA5 or PA6, depending on which array measures the peak flux.

4.3. Counterparts

We searched for counterparts for each transient event in the SIMBAD³⁴ (Wenger et al. 2000) database. The results of this search are summarized in Table 5. We searched for any Gaia objects (Mou & Webster 2021) within 1' of each event and list the SIMBAD identification. We calculate the probability of a chance association given the density of Gaia stars (Mou & Webster 2021) with the counterpart's magnitude or lower within the counterpart's separation of the transient's position. We exclude any counterparts with a chance association probability greater than 10%. We also searched for counterparts of the transients found in Naess et al. (2021a), which are recovered in this analysis. The associations agree with the original findings.

In addition to the Gaia source catalog, we search for galactic objects in the Gaia extragalactic catalog (Mou & Webster 2021) using VizieR (Ochsenbein et al. 2000). Only events 10 and 14 have associations from this catalog. Event 10 is coincident with an AGN with a 1.1% chance of a false association (see

Table 5). Event 14 is coincident with a RR Lyrae star with a 2.4% chance of a false association. This association is not listed because there is a much more obvious Gaia star associated with event 14.

In Figure 8 we plot the positions of the transients overlaid on combined ACT data from 2007–2019. This plot includes color images in the optical from the Digitized Sky Surveys (DSS)^{35,36} that show there are bright stellar counterparts for most of the events.

5. Discussion and Conclusions

We have demonstrated a pipeline of transient detection and characterization using ACT data, and presented a catalog of 21 mm transients from 3 day maps, including three of which were previously detected, and four events that cannot be confirmed as real transients. After assessing the spectral indices and counterpart associations of these events, two classes of objects emerge: flares associated with stars with flat or falling spectra, indicating radiation from synchrotron emission, and stellar flares with rising spectra, indicating thermal emission.

³⁵ https://archive.stsci.edu/cgi-bin/dss_form

³⁶ These images were acquired using the online tool Aladin Lite. See Boch & Fernique (2014).

³⁴ <https://simbad.cds.unistra.fr/simbad/>

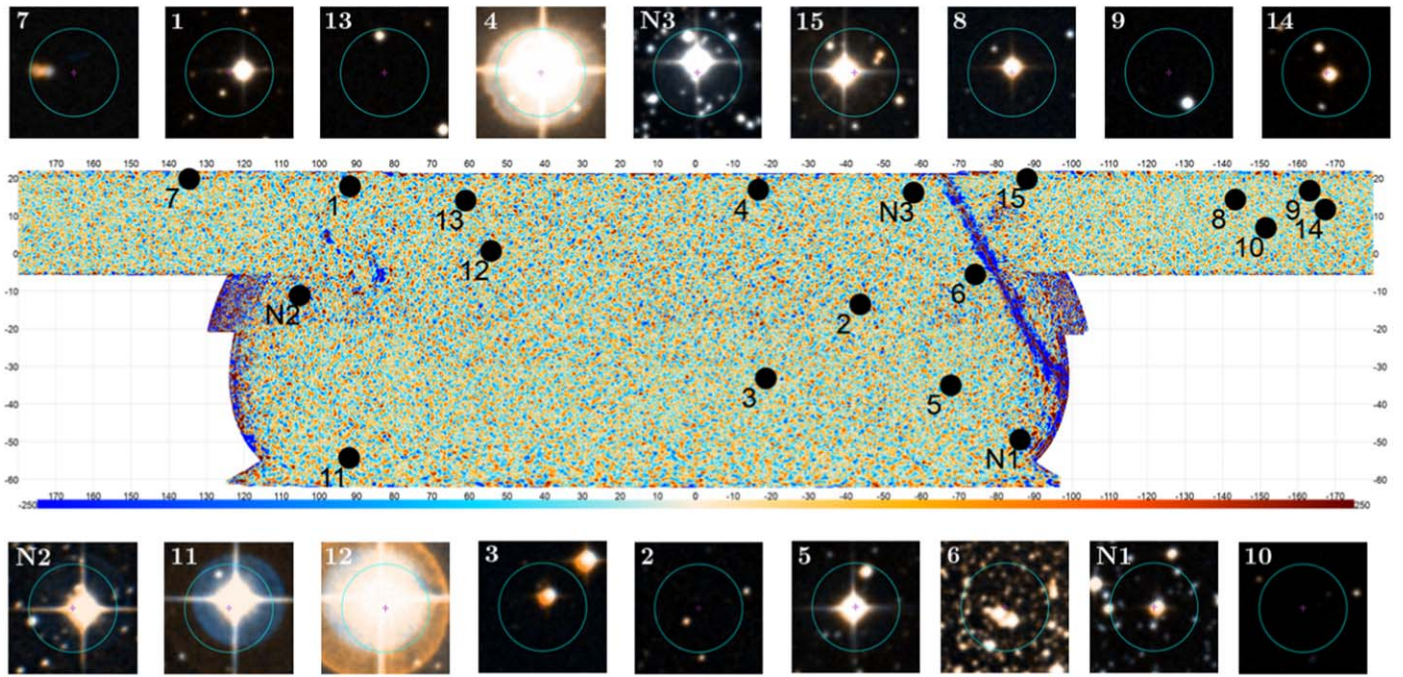


Figure 8. Combined ACT data from 2007–2019 overlaid with the transient positions. Images from DSS at each location, indicated by a + sign in the center of each image, are also shown with a 1' contour plotted for scale. The majority of the transient events have bright stellar counterparts seen in the optical.

Performing a statistical analysis on such a small sample size is difficult, but in the future as we discover more millimeter stellar transients, we will be able to better characterize them. For example, we will be able to determine whether these events reside near the galactic plane or scattered across the sky, or whether two classes of transients, rising versus falling spectra, really exist, or if there is simply a wide distribution of spectral indices. Tests of these statistics with our small number of events are inconclusive.

Events 3, 4a, 4b, 5a, 5b, 11, 12a, 12b, and 15 are associated with rotating variable stars. These stars have large dark spots on their surface from magnetic activity in their chromospheres. These spots cause intrinsic variability in flux in optical and IR wavelengths but also cause flares in radio wavelengths from synchrotron radiation (Hjellming & Gibson 1980). Events 4, 11, 12, and 15 are coincident with a special type of rotating variable stars called RS Canum Venaticorum variables. These are binary systems that also exhibit variability due to dark spots (see Hall 1976; Zeilik et al. 1979). Similar events were seen in the millimeter systematic transient search from SPT-3G (Guns et al. 2021).

Event 1 is also associated with a binary system. Although it is not classified as rotationally variable, it most likely flares in the microwave with a similar mechanism. This association is similar to ACT-T J200758+160954 (N3) which was previously published in Naess et al. (2021a).

Events 7, 8, and 15 are all coincident with cool G-, K-, and M-type stars. Event 14 is associated with a Gaia star but its spectral type is unknown. Since all of these events also have negative spectral indices, these flares are most likely from magnetic activity producing synchrotron radiation. This is consistent with findings from Guns et al. (2021) who reported microwave flares from M and K dwarfs. These cool stars have convective envelopes, which cause increased magnetic activity but do not exhibit the same dark spots found in rotationally variable stars (Yang et al. 2017).

Events 6, N1, and N2 all have rising spectra, which are associated with thermal emission. In these cases, some mechanism other than synchrotron radiation is driving the flares. N1 and N2 are associated with cool M and K stars, respectively, but the spectral types of the star associations for 6 and 9 are unknown. Guns et al. (2021) also observed two events with M-dwarf counterparts with rising spectra indicating this is a common class of millimeter transients.

Although we cannot be certain events 2, 9, 10, and 13 are real transients, we still present possible counterparts for them in Table 5. There is a 6% chance that the Gaia counterpart for event 2 is a chance association. If the association is correct this transient is likely due to synchrotron radiation from stellar magnetic fields. The field around Event 10 is too dense to pinpoint a stellar counterpart. However, there is a small chance this event is associated with an AGN. Eftekhari et al. (2022) predict ACT will see on the order of 10 GRBs but this event is not associated with any known GRB flares listed in the Fermi All-sky Variability Analysis (Abdollahi et al. 2017). The associations for events 9 and 13, are also unclear. Both events have rising spectra so they would most likely be similar to events 6, N1, and N2. The Zwicky Transient Facility (ZTF; Masci et al. 2018) detected a flare with the same Gaia counterpart associated with event 13 twelve days after and 23'' away from the ACT detection. ZTF also detects repeating flares that are 34'' away from Event 9, although they did not occur close in time to the ACT detection.³⁷

This sample likely only represents a fraction of microwave transient events present in the ACT data. The 3 day maps were not made for a systematic transient search. Recently, single observation maps that span more seasons than the 3 day maps have been made for the purpose of an ACT time-domain study. Major advantages of the single observation maps include the

³⁷ This cross detection was done using software developed by Matheson et al. (2021).

relative consistency in noise performance in each map, thus decreasing the likelihood of over-cutting our initial transient detections, and the freedom of stacking single scan maps for different periods of time. We will perform a similar analysis to search for transient events within those maps to gain a more accurate event rate for ACT. This will inform current and future large sky-area millimeter surveys such as SPT (Carlstrom et al. 2011), Simons Observatory (Ade et al. 2019), CCAT-prime (Aravena et al. 2023), and CMB-S4 (Abazajian et al. 2019) on how to best detect and study these events. In particular, the SO (and Advanced SO) large aperture telescope, or SO LAT, will be outfitted with 10 (20) times the number of detectors as ACT, increasing the sensitivity to be a factor of $\sqrt{10}$ better than ACT maps. SO LAT will also have a larger field of view and a more regular cadence than ACT further improving its ability as a transient detector.

Acknowledgments

The Authors would like to thank Carles Badenes for the helpful discussions and comments.

This work was supported by the U.S. National Science Foundation through awards AST-0408698, AST-0965625, and AST-1440226 for the ACT project, as well as awards PHY-0355328, PHY-0855887, and PHY-1214379. Funding was also provided by Princeton University, the University of Pennsylvania, and a Canada Foundation for Innovation (CFI) award to UBC. ACT operates in the Parque Astronómico Atacama in northern Chile under the auspices of the Agencia Nacional de Investigación y Desarrollo (ANID; formerly Comisión Nacional de Investigación Científica y Tecnológica de Chile, or CONICYT).


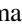

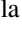
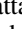
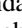
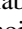


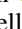






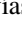

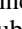
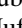

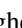
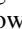


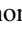
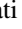





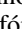

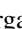
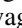
Computations were performed using Princeton Research Computing resources at Princeton University. This research has made use of data and/or services provided by the International Astronomical Union's Minor Planet Center. This research has made use of the SIMBAD database, operated at CDS, Strasbourg, France.

Y.L. acknowledges support from the KIC Postdoctoral Fellowship. This work was supported by a grant from the Simons Foundation (CCA 918271, PBL). E.C. acknowledges support from the European Research Council (ERC) under the European Union's Horizon 2020 research and innovation program (grant agreement No. 849169). S.K.C. acknowledges support from NSF award AST-2001866. R.D. thanks CONICYT for grant BASAL CATA FB210003. C.H.C. acknowledges the FONDECYT Postdoc fellowship 3220255. A.D.H. acknowledges support from the Sutton Family Chair in Science, Christianity and Cultures and from the Faculty of Arts and Science, University of Toronto. K.M.H. acknowledges support by NSF awards AST-1815887 and AST-2206344. J.P.H. gratefully acknowledges support from the estate of George A. and Margaret M. Downsbrough. C.S. acknowledges support from the Agencia Nacional de Investigación y Desarrollo (ANID) through FONDECYT grant No. 11191125 and BASAL project FB210003. E.M.V. acknowledges support from NSF award AST-2202237.

The Digitized Sky Surveys were produced at the Space Telescope Science Institute under US Government grant NAG W-2166. The images of these surveys are based on photographic data obtained using the Oschin Schmidt Telescope on Palomar Mountain and the UK Schmidt Telescope. The plates were processed into the present compressed digital form with

the permission of these institutions. This research has made use of the Aladin Sky Atlas developed at CDS, Strasbourg Observatory, France. This research has made use of the VizieR catalog access tool, CDS, Strasbourg, France (doi: 10.26093/cds/vizieR). The original description of the VizieR service was published in Ochsenbein et al. (2000).

ORCID iDs

Yaqiong Li  <https://orcid.org/0000-0001-8093-2534>
 Emily Biermann  <https://orcid.org/0000-0002-2840-9794>
 Sigurd Naess  <https://orcid.org/0000-0002-4478-7111>
 Simone Aiola  <https://orcid.org/0000-0002-1035-1854>
 Nicholas Battaglia  <https://orcid.org/0000-0001-5846-0411>
 Tanay Bhandarkar  <https://orcid.org/0000-0002-2971-1776>
 Erminia Calabrese  <https://orcid.org/0000-0003-0837-0068>
 Steve K. Choi  <https://orcid.org/0000-0002-9113-7058>
 Kevin T. Crowley  <https://orcid.org/0000-0001-5068-1295>
 Mark Devlin  <https://orcid.org/0000-0002-3169-9761>
 Cody J. Duell  <https://orcid.org/0000-0002-6318-1924>
 Shannon M. Duff  <https://orcid.org/0000-0002-9693-4478>
 Jo Dunkley  <https://orcid.org/0000-0002-7450-2586>
 Rolando Dünner  <https://orcid.org/0000-0003-3892-1860>
 Patricio A. Gallardo  <https://orcid.org/0000-0001-9731-3617>
 Yilun Guan  <https://orcid.org/0000-0002-1697-3080>
 Carlos Hervías-Caimapo  <https://orcid.org/0000-0002-4765-3426>
 Adam D. Hincks  <https://orcid.org/0000-0003-1690-6678>
 Johannes Hubmayr  <https://orcid.org/0000-0002-2781-9302>
 Kevin M. Huffenberger  <https://orcid.org/0000-0001-7109-0099>
 John P. Hughes  <https://orcid.org/0000-0002-8816-6800>
 Arthur Kosowsky  <https://orcid.org/0000-0002-3734-331X>
 Thibaut Louis  <https://orcid.org/0000-0002-6849-4217>
 Maya Mallaby-Kay  <https://orcid.org/0000-0002-2018-3807>
 Jeff McMahon  <https://orcid.org/0000-0002-7245-4541>
 Federico Nati  <https://orcid.org/0000-0002-8307-5088>
 Michael D. Niemack  <https://orcid.org/0000-0001-7125-3580>
 John Orłowski-Scherer  <https://orcid.org/0000-0003-1842-8104>
 Lyman Page  <https://orcid.org/0000-0002-9828-3525>
 Maria Salatino  <https://orcid.org/0000-0003-4006-1134>
 Cristóbal Sifón  <https://orcid.org/0000-0002-8149-1352>
 Suzanne T. Staggs  <https://orcid.org/0000-0002-7020-7301>
 Cristian Vargas  <https://orcid.org/0000-0001-5327-1400>
 Eve M. Vavagiakis  <https://orcid.org/0000-0002-2105-7589>
 Yuhan Wang  <https://orcid.org/0000-0002-8710-0914>
 Edward J. Wollack  <https://orcid.org/0000-0002-7567-4451>

References

- Abazajian, K., Addison, G., Adshead, P., et al. 2019, arXiv:1907.04473
 Abbott, B., Abbott, R., Abbott, T., et al. 2016, *PhRvL*, **116**, 061102
 Abdollahi, S., Ackermann, M., Ajello, M., et al. 2017, *ApJ*, **846**, 34
 Ade, P., Aguirre, J., Ahmed, Z., et al. 2019, *JCAP*, **2019**, 056
 Aghanim, N., Akrami, Y., Arroja, F., et al. 2020, *A&A*, **641**, A1
 Aiola, S., Calabrese, E., Maurin, L., et al. 2020, *JCAP*, **2020**, 047
 Aravena, M., Austermann, J. E., (CCAT-Prime Collaboration), et al. 2023, *ApJS*, **264**, 7
 Boch, T., & Fernique, P. 2014, in ASP Conf. Ser. 485, *Astronomical Data Analysis Software and Systems XXIII*, ed. N. Manset & P. Forshay (San Francisco, CA: ASP), 277
 Bower, G. C., Plambeck, R. L., Bolatto, A., et al. 2003, *ApJ*, **598**, 1140

- Brown, J. M., & Brown, A. 2006, *ApJL*, **638**, L37
- Carlstrom, J. E., Ade, P. A. R., Aird, K. A., et al. 2011, *PASP*, **123**, 568
- Chen, X., Rachen, J. P., López-Cañego, M., et al. 2013, *A&A*, **553**, A107
- Choi, S. K., Austermann, J., Beall, J. A., et al. 2018, *JLTP*, **193**, 267
- Christy, C. T., Jayasinghe, T., Stanek, K. Z., et al. 2022, *PASP*, **134**, 024201
- Dünner, R., Hasselfield, M., Marriage, T. A., et al. 2012, *ApJ*, **762**, 10
- Eftekhari, T., Berger, E., Metzger, B. D., et al. 2022, *ApJ*, **935**, 16
- Fowler, J. W., Niemack, M. D., Dicker, S. R., et al. 2007, *ApOpt*, **46**, 3444
- Granot, J., & Sari, R. 2002, *ApJ*, **568**, 820
- Guns, S., Foster, A., Daley, C., et al. 2021, *ApJ*, **916**, 98
- Hall, D. S. 1976, in *IAU Colloq. 29, Multiple Periodic Variable Stars* (Cambridge: Cambridge Univ. Press), 287
- Hervías-Caimapo, C., Naess, S., Hincks, A. D., et al. 2023, arxiv:2301.07651
- Hjellming, R. M., & Gibson, D. M. 1980, in *IAU Symp. 86, Radio Physics of the Sun*, ed. M. R. Kundu & T. E. Gergely (Cambridge: Cambridge Univ. Press), 209
- Ho, A. Y. Q., Phinney, E. S., Ravi, V., et al. 2019, *ApJ*, **871**, 73
- Ho, S.-P. P., Austermann, J., Beall, J. A., et al. 2017, *Proc. SPIE*, 9914, 991418
- Ivezić, Ž., Kahn, S. M., Tyson, J. A., et al. 2019, *ApJ*, **873**, 111
- Kuno, N., Sato, N., Nakanishi, H., et al. 2004, *PASJ*, **56**, L1
- Laskar, T., Alexander, K. D., Gill, R., et al. 2019, *ApJL*, **878**, L26
- MacGregor, A. M., Osten, R. A., & Hughes, A. M. 2020, *ApJ*, **891**, 80
- Mairs, S., Lalchand, B., Bower, G. C., et al. 2019, *ApJ*, **871**, 72
- Masci, F. J., Laher, R. R., Rusholme, B., et al. 2018, *PASP*, **131**, 018003
- Massi, M., Forbrich, J., Menten, K. M., et al. 2006, *A&A*, **453**, 959
- Matheson, T., Stubens, C., Wolf, N., et al. 2021, *AJ*, **161**, 107
- Mou, J., & Webster, I. 2021, Davida, <https://www.spacereference.org/asteroid/511-davida-a903-kb>
- Naess, S., Aiola, S., Battaglia, N., et al. 2021b, *ApJ*, **923**, 224
- Naess, S., Battaglia, N., Richard Bond, J., et al. 2021a, *ApJ*, **915**, 14
- Ochsenbein, F., Bauer, P., & Marcout, J. 2000, *A&AS*, **143**, 23
- Orlowski-Scherer, J., Venterea, R., Battaglia, N., et al. 2023, arxiv:2306.05468
- Rowlinson, A., Meijn, J., Bright, J., et al. 2022, *MNRAS*, **517**, 2894
- Thornton, R. J., Ade, P. A. R., Aiola, S., et al. 2016, *ApJS*, **227**, 21
- Wenger, M., Ochsenbein, F., Egret, D., et al. 2000, *A&AS*, **143**, 9
- Whitehorn, N., Natoli, T., Ade, P. A. R., et al. 2016, *ApJ*, **830**, 143
- Yang, H., Liu, J., Gao, Q., et al. 2017, *ApJ*, **849**, 36
- Yuan, Q., Wang, Q. D., Lei, W.-H., Gao, H., & Zhang, B. 2016, *MNRAS*, **461**, 3375
- Zeilik, M., Hall, D. S., Feldman, P. A., & Walter, F. 1979, *S&T*, **57**, 132